Nonclassical Crystal Growth of Supramolecular Polymers in Aqueous Medium

Drishya Elizebath, Jia Hui Lim, Yoshiharu Nishiyama, Balaraman Vedhanarayanan, Akinori Saeki, Yu Ogawa, Vakayil Praveen

Nonclassical Crystal Growth of Supramolecular Polymers in Aqueous Medium

Drishya Elizebath,[a, b] Jia Hui Lim,[c] Yoshiharu Nishiyama,[c] Balaraman Vedhanarayanan,[a] Akinori Saeki,[d] Yu Ogawa,[c] and Vakayil K. Praveen*[a, b]*

D. Elizebath, Dr. B. Vedhanarayanan, Dr. V. K. Praveen
Chemical Sciences and Technology Division, CSIR-National Institute for Interdisciplinary Science and Technology (CSIR-NIIST), Thiruvananthapuram, Kerala 695019, India
E-mail: vkpraveen@niist.res.in

D. Elizebath, Dr. V. K. Praveen
Academy of Scientific and Innovative Research (AcSIR), Ghaziabad-201002, India

J. H. Lim, Dr. Y. Nishiyama, Dr. Y. Ogawa
Univ. Grenoble Alpes, CNRS, CERMAV, Grenoble 38000, France
E-mail: yu.ogawa@cermav.cnrs.fr

Prof. Dr. A. Saeki
Department of Applied Chemistry, Graduate School of Engineering, Osaka University, Suita, Osaka 565-0871, Japan

Keywords: self-assembly, supramolecular polymer, order, nonclassical crystallization, 3D electron diffraction

Abstract: Mechanistic understanding of the principles governing the hierarchical organization of supramolecular polymers offers a paradigm for tailoring synthetic molecular architectures at the nano to micrometric scales. Herein, we demonstrate the unconventional crystal growth mechanism of a supramolecular polymer of superbenzene(coronene)-diphenylalanine conjugate (**Cr-FF$_{OEt}$**). Three-dimensional electron diffraction (3D ED), a technique underexplored in supramolecular chemistry, was effectively utilized to gain a molecular-level understanding of the gradual growth of the initially formed poorly crystalline hairy, fibril-like supramolecular polymers into the ribbon-like crystallites. The further evolution of these nanosized ribbons into microcrystals by oriented attachment and lateral fusion was probed by time-resolved microscopy and electron diffraction. The gradual morphological and structural changes reveal the nonclassical crystallization pathway, where the balance of strong and weak

intermolecular interactions led to a structure beyond the nanoscale. The role of distinct π-stacking and H-bonding interactions that drive the nonclassical crystallization process of **Cr-FF$_{OEt}$** supramolecular polymers was analyzed in comparison to analogous molecules, **Py-FF$_{OEt}$** and **Cr-FF** forming left- and right-handed twisted fibers, respectively. Furthermore, the **Cr-FF$_{OEt}$** crystals formed through nonclassical crystallization were found to improve the functional properties.

1. Introduction

One of the predominant leitmotifs of the hierarchically organized biopolymers is the "pre-programmed" chemical entities that could forecast their precise structure and functions.[1] A great deal of effort in mimicking natural systems led to the development of supramolecular polymers.[2] Akin to biopolymers, the molecular building blocks of supramolecular polymers can predict the outcome of competing intermolecular interactions and provide the possibility of exploring new coordinates of the free energy landscape.[3,4] Studies in this direction not only unraveled mechanistic insights but also provided methods for creating supramolecular structures under kinetic control.[5,6] However, leveraging the pathway complexity and integrating the supramolecular polymers into the mesoscale requires adequate building strategies.[7] For instance, nonclassical crystallization that utilizes various intermediate structures other than atoms, ions, and molecules[8,9] provides a feasible approach to material fabrication based on supramolecular polymers.

The classical crystallization theory considers the crystalline nucleation and growth process by simple monomer-by-monomer addition without many structural changes in the bulk or at the surface. However, numerous examples of crystallization in biological[10] and geological[11] systems challenge the classical model and are readily explained with the nonclassical nucleation and growth models. The nonclassical, multistep crystallization model involves either a prenucleation cluster formation or follows a particle assembly pathway, which highlights the diversity and complexity of the process and has been widely studied in recent years.[8-12] During the advanced stages of crystallization, the nonclassical crystal growth via oriented particle attachment and mesocrystal formation is frequently observed.[x] Although particle-based crystal growth is common in inorganic and protein crystallization, only a few reports on organic dye-based systems are known.[12] Recently, Rybtchinski and co-workers have demonstrated the supramolecular polymers of an organic molecule could act as potential building blocks in the nonclassical crystallization pathway.[12b,c] However, a molecular-level understanding that could forecast the crystal growth pathway is currently lacking in the supramolecular systems.

Extrapolating the general features of nonclassical crystallization mechanisms to supramolecular polymers could aid the formation of nanostructures and their spontaneous long-range alignment towards

the construction of materials in mesoscale. It is envisaged that supramolecular polymers with favorable surface topologies could promote interpolymer interactions and the gradual evolution of order across different length scales.[14] Herein, we demonstrate the nonclassical crystal growth pathway adopted by the supramolecular polymer fibrils of superbenzene (coronene)-dipeptide conjugate via flat ribbons to crystals. The molecular packing in the crystal originating from the specific molecular interactions was unraveled by 3D ED,[15] a method relatively underexplored in the field of supramolecular chemistry.[16] Interestingly, varying the hydrophilic/hydrophobic balance of the molecular structure led to the formation of helical and twisted structures that remained in the fibrillar morphology.

2. Results and Discussion

2.1. Self-assembly behavior of Cr-FF$_{OEt}$ and Py-FF$_{OEt}$

The molecules **Cr-FF$_{OEt}$** and **Py-FF$_{OEt}$** consist of a coronene and pyrene moiety, respectively conjugated to the *N*-terminal of a *C*- protected diphenylalanine (FF$_{OEt}$) via a butyl chain linker (**Figure 1**). In contrast, **Cr-FF** contains a *C*-terminal deprotected diphenylalanine while maintaining the rest of the molecular structure of **Cr-FF$_{OEt}$** (**Figure 1**). These molecules were synthesized following the multistep synthesis strategy outlined in Scheme S1 and S2 and were characterized by FT-IR, ^{1}H, and ^{13}C NMR spectroscopy and high-resolution mass spectrometry (see Supporting Information).

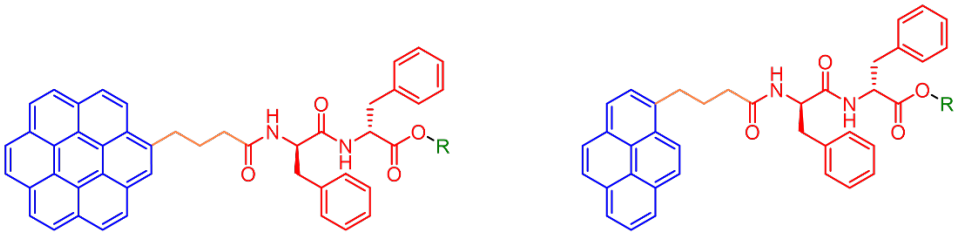

Figure 1. Chemical structure of coronene dipeptide (**Cr-FF$_{OEt}$** and **Cr-FF**) and pyrene dipeptide (**Py-FF$_{OEt}$**) conjugates.

To explore the self-assembling behavior of **Cr-FF$_{OEt}$** and **Py-FF$_{OEt}$**, they were first dissolved in a good solvent (THF) and then diluted with water (**Figure 2a**). The aggregation process was then monitored using spectroscopy techniques. **Cr-FF$_{OEt}$** in THF ($c_T = 5 \times 10^{-5}$ M) showed UV-vis spectral features signature to that of the monomerically dissolved state with an absorption maximum at 304 nm

(**Figure 2b**). Furthermore, **Cr-FF$_{OEt}$** in THF displayed a photoluminescence spectrum with well-resolved vibronic features (λ_{max} = 429 nm) and a monoexponential lifetime decay, τ = 28.63 ns (**Figure S1**). When diluting the **Cr-FF$_{OEt}$** solution in THF with water at a concentration of $c_T = 5 \times 10^{-5}$ M of **Cr-FF$_{OEt}$** in water/THF (6:4 v/v), a gradual hypochromic effect occurred in the UV-vis absorption, indicating the aggregation induced by the solvent exchange (**Figure S2**). Compared to the UV-vis spectral features of the monomerically dissolved **Cr-FF$_{OEt}$**, solvent replacement into water (6:4 v/v) leads to a significant broadening of absorption over a period of 1 h (**Figure 2b** and **Figure S3**). The aggregation processes led to the appearance of bands at the longer wavelength region (357, 371, and 411 nm). The photoluminescence spectrum of the corresponding aggregates was broad with a significant red-shift (λ_{max} = 491 nm), and the average lifetime (τ_{av}) value was significantly enhanced to 58.19 ns (**Figure S4**).[17]

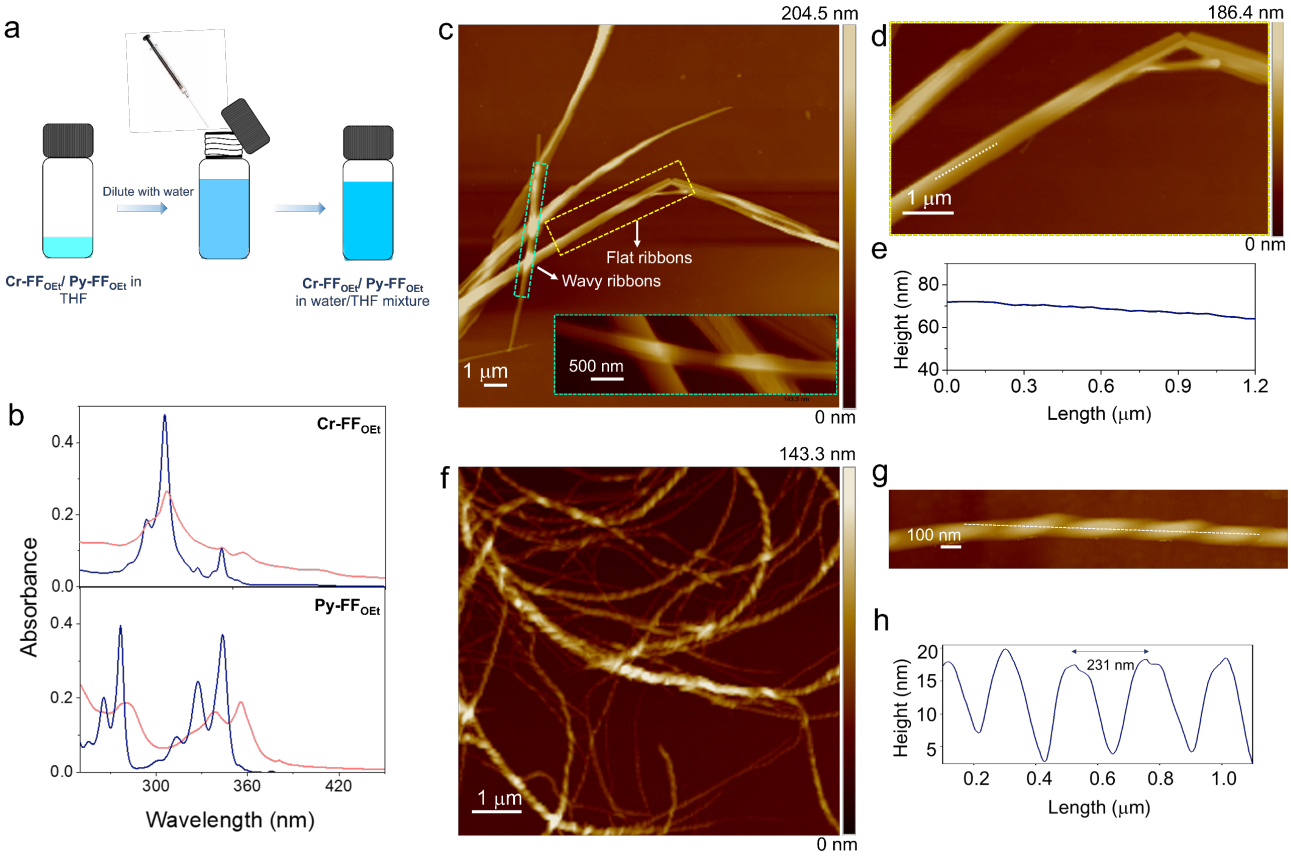

Figure 2. (a) Sample preparation procedure followed for the self-assembly of **Cr-FF$_{OEt}$** and **Py-FF$_{OEt}$.** (b) UV-vis absorption spectra of **Cr-FF$_{OEt}$** ($c_T = 5 \times 10^{-5}$ M) in THF (blue) and aggregates in water/THF (6:4 v/v, red) at 25 °C; **Py-FF$_{OEt}$** ($c_T = 5 \times 10^{-5}$ M) in THF (blue) and aggregates in water/THF (7:3 v/v, red) at 25 °C. (c) AFM height image of **Cr-FF$_{OEt}$** aggregates in water/THF (6:4 v/v, $c_T = 5 \times 10^{-5}$ M) at 25 °C and inset shows the magnified AFM image of the greenish-blue box. (d) Magnified AFM height images of the yellow box in Figure 2c. (e) Cross-sectional analysis along the white dotted line shown in Figure 2d. (f) AFM height image of **Py-FF$_{OEt}$** helical nanofibers in water/THF (7:3 v/v, $c_T = 5 \times 10^{-5}$ M) at 25 °C. (g) AFM height images of a single helical fiber. (h) Cross-sectional analysis along the white dotted line shown in Figure 2g depicts the pitch of helical fibers.

Interestingly, **Py-FF$_{OEt}$**, which contains pyrene with a lower carbon-to-hydrogen ratio in comparison to coronene, aggregated at a high-water content (water/THF; 7:3 v/v $c_T = 5 \times 10^{-5}$ M) (**Figure 2b** and **Figure S5**). Upon aggregation, the vibronically well-resolved absorption and photoluminescence spectra of **Py-FF$_{OEt}$** in THF underwent a bathochromic shift with a spectral broadening. Furthermore, the lifetime value was significantly reduced from $\tau = 21.17$ ns (monomer) to $\tau_{av} = 9.04$ ns (aggregate) (**Figure S6**). Atomic force microscopy (AFM) analyses revealed distinct morphologies of **Cr-FF$_{OEt}$** and **Py-FF$_{OEt}$**. **Cr-FF$_{OEt}$** showed a mixed population of wavy and flat ribbons (**Figure 2c-e** and **Figure S7**). The flat ribbons were devoid of any chiral appearance, i.e., twisting (**Figure 2d,e**). **Py-FF$_{OEt}$** displayed the formation of left-

handed helical fibers having heights ranging from 80-300 nm and lengths of several micrometers (**Figure 2f** and **Figure S8**). These fibers showed a well-defined twist with a pitch of ca. 230 nm (**Figure 2g,h**)

During the assembly process of **Cr-FF$_{OEt}$**, the appearance of the solution significantly changed over the course of 12 h after the addition of water, where the turbid solution transformed into suspensions of visible needle-like particles (**Figure S9**). These micrometer-long needle-like aggregates showed strong birefringence, indicating the crystalline nature and strong orientation of the crystal domains of **Cr-FF$_{OEt}$** aggregates (**Figure S10**).[18] AFM and transmission electron microscopy (TEM) studies revealed that the width and height of the ribbons increased continuously over the same time period (**Figure S11**). In contrast, the suspension of **Py-FF$_{OEt}$** showed no such change over time and remained in their helical morphology (**Figure S12a,b**). Similarly, the bright field image and the corresponding images of **Py-FF$_{OEt}$** under crossed polarizers showed negligible birefringence compared to that of **Cr-FF$_{OEt}$** microcrystals (**Figure S12c,d)**.

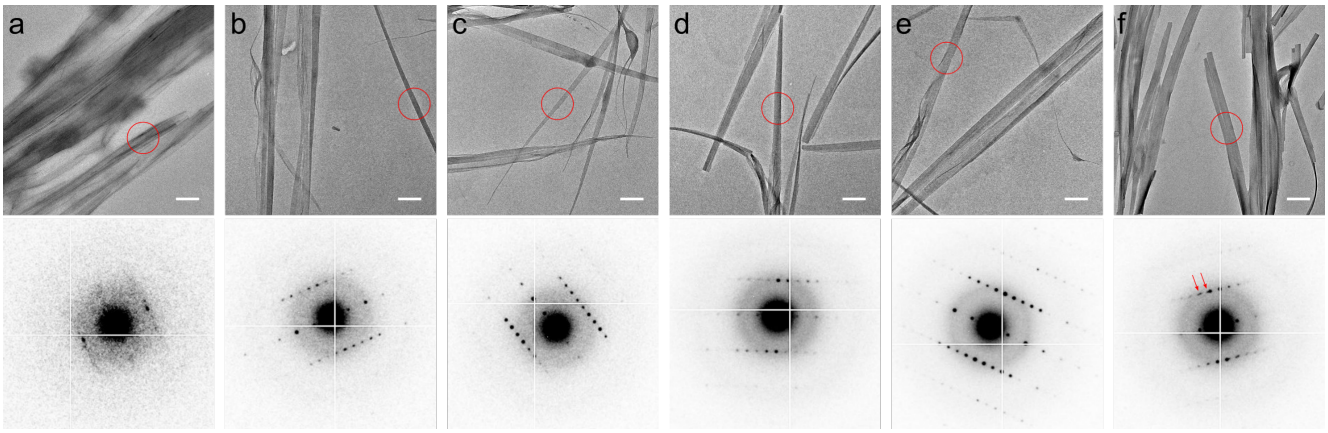

Figure 3. Evolution of fibrillar assemblies of **Cr-FF$_{OEt}$** in water/THF (6:4 v/v, $c_T = 5 \times 10^{-5}$ M) at 25 °C. TEM images (top) and ED patterns obtained from the circled area (bottom) of specimens prepared (a) 5 min, (b) 10 min, (c) 30 min, (d) 1 h, (e) 2 h, and (f) 4 h after the solvent switch. The asymmetry of the ED patterns is due to the slight tilt of the crystallites. Scale bar = 500 nm.

The evolution of the assembly process of **Cr-FF$_{OEt}$** was further monitored using TEM and electron diffraction (ED). The specimen, after 5 min of aging, shows the formation of thin hairy 1D fibrillar structures having a width of 10-30 nm (**Figure 3a**). These thin fibers provided poorly resolved ED patterns and thus possessed small crystalline domains with disordered molecular packing. These fibers tend to laterally assemble into loose bundles of a width of a few hundred nanometers (**Figure 3b**). The fibrillar structures grew into ribbon-like crystallites with a broad width distribution ranging from 30 to 200 nm in the next few hours. These ribbons yielded well-defined spot ED patterns as shown in the 1 and 2 h samples and are thus single crystalline. (**Figure 3c-e**). Longer crystallization, 4 h time, resulted in thicker ribbons with diameters often larger than a few hundred nanometers (**Figure 3f**). These structures are not single

crystalline as their ED patterns were often contained reflections from multiple and slightly misaligned crystal domains in single ED diagrams (red arrows in **Figure 3f**). This observation indicates that these larger fibers formed via the oriented attachment of the smaller crystalline fibers. The single-crystalline thin ribbons were likely laterally stacked to form these thicker ribbons. After 4 h, larger aggregates with diameters of micrometers became predominant, which were too large for TEM ED studies.

To evaluate the topological features of the microcrystals obtained after 12 h of aging, the samples were subjected to field emission scanning electron microscopy (FE-SEM) and AFM. The FE-SEM images showed microcrystals with a length of 300 ± 60 μm and a width of 2 ± 1 μm (**Figure 4a** and **Figure S13**). The magnified FE-SEM images of the microcrystal (**Figure 4b, c**) and its fractured surface (**Figure 4c, d**) revealed the laterally stacked microribbons (2D layers) aligned parallel to the longitudinal axis of microcrystals. AFM height and phase images also showed the multilamellar features of the microcrystals (**Figure 4e-g**). The fluorescence microscopic image of the microcrystals under excitation at 330-380 nm exhibited bright green fluorescence (**Figure 4h**). The fusion of the ribbon structures is visible on the tip of the microcrystal (inset of **Figure 4h**). The combination of the morphological and ED-based analyses indicates that the micron-sized crystalline fibers of **Cr-FF$_{OEt}$** formed through a nonclassical crystal growth process, as schematically represented in **Figure 4i**. The poorly crystalline hairy ribbons act as basic building blocks and fuse into single crystalline ribbons. These single-crystalline flat ribbons further assemble into larger micron-sized fibrous aggregates.

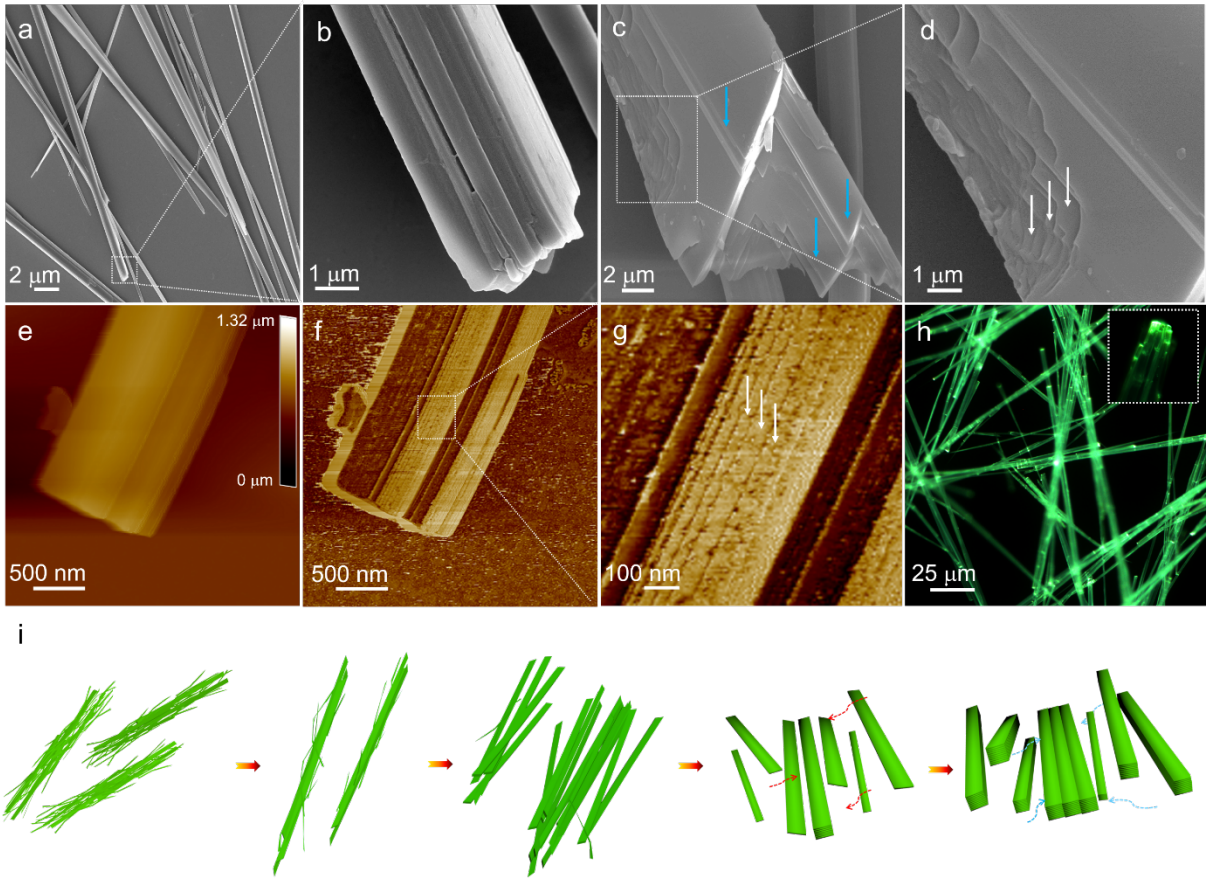

Figure 4. FE-SEM images of (a) microcrystals of **Cr-FF$_{OEt}$**, (b) magnified image of the microcrystal showing the longitudinal attachment of microribbons, (c) magnified image of a fractured microcrystal (side-to-side attachment of microribbons is indicated by blue arrows), and (d) magnified image of the white dotted box of Figure 4c, showing the parallel stacking of 2D layers (lamellation-indicated by white arrows). AFM images of microcrystal (e) AFM height image of a microcrystal (f) corresponding phase image, (g) magnified phase image showing the lamellation of 2D layers (indicated by white arrows). (h) Fluorescence microscopy image of the microcrystals excited at 330-380 nm: inset shows a magnified image showing the side-to-side attachment of flat microribbons. (i) Schematic representation of the nonclassical crystallization pathway adopted by **Cr-FF$_{OEt}$**.

2.2. 3D ED analysis of Cr-FF$_{OEt}$ microcrystals

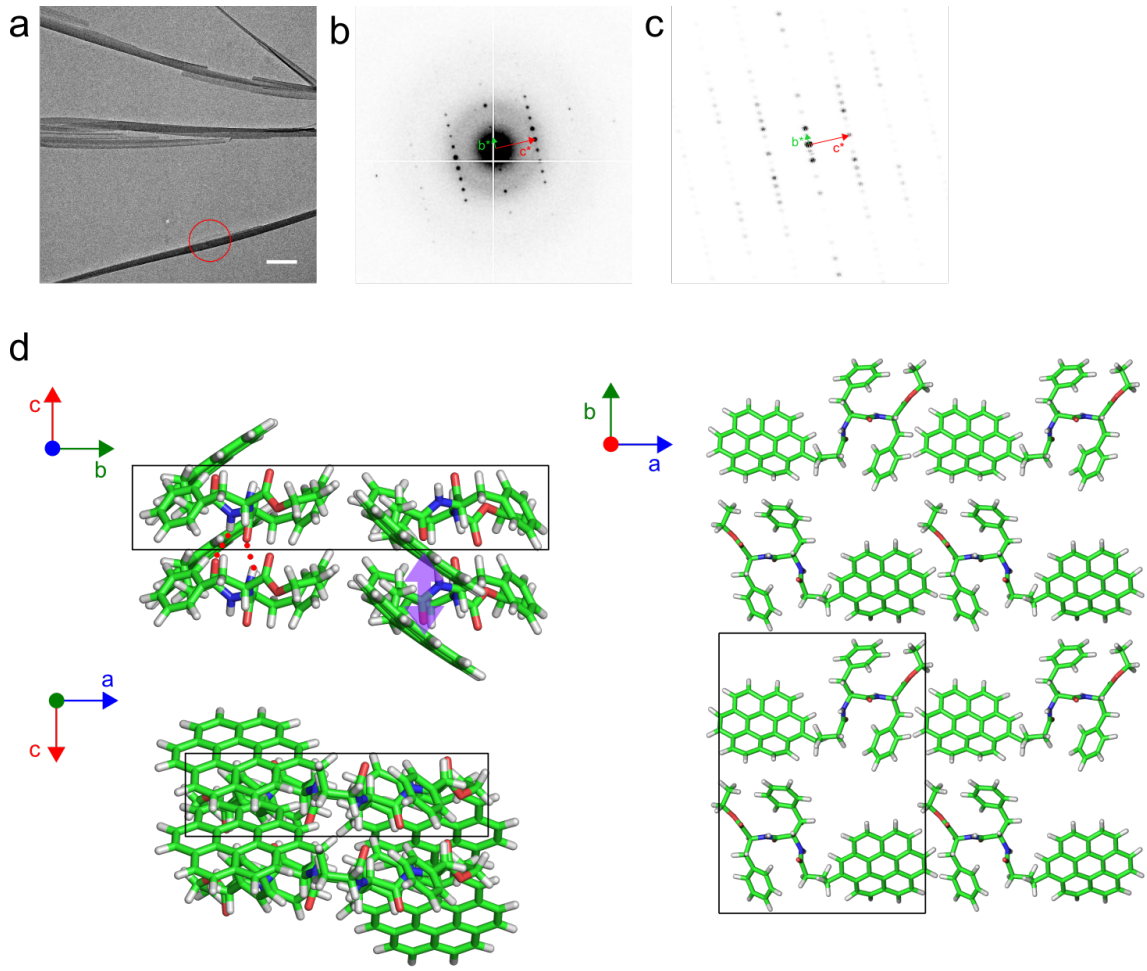

Figure 5. 3D ED analysis of **Cr-FF$_{OEt}$** crystal structure. (a) Diffraction contrast image (left) and a representative base-plane ED diagram corresponding to [1 0 0] zone axis pattern. Scale bar = 500 nm. A comparison between (b) experimental and (c) simulated patterns based on the packing model. (d) Packing model of **Cr-FF$_{OEt}$** crystal.

We employed the 3D ED technique to get an insight into the molecular interactions leading to the observed nonclassical crystallization of **Cr-FF$_{OEt}$**. A nanoribbon with a width of ca. 50 nm yielded high-resolution spot ED patterns with a resolution close to 1 Å (**Figure 5a,b**). Representative 2D ED patterns at different tilt angles are shown in **Figure S14**. The reconstruction of ED intensity data in 3D space allowed us to determine the unit cell (**Figure S15,16**). The unit cell is orthorhombic with parameters a = 18.1 Å, b = 24.5 Å, and c = 4.95 Å, with c-axis corresponding to the fiber and supramolecular polymer chain axis. The systematic absence indicates the two-fold symmetry along the b-axis but not in the other directions. Thus, the space group is likely $P2_1$. This non-orthorhombic, low-symmetry space group implies that the unit cell is indeed pseudo-orthorhombic, and the crystal structure is originally monoclinic with a unique axis being the b-axis. The transition from monoclinic to orthorhombic systems is likely due to the assembly process of smaller imperfect crystallites assembled into larger single crystalline ribbons.

If the crystallites with opposite directionalities merge into one single crystal, the mergers should make the monoclinic angle closer to 90° to match contacting surfaces, resulting in the pseudo-orthorhombic structure. While this intrinsic twinning prevents us from the crystallographic structure refinement, the unit cell and 3D ED patterns provide valuable insights into the packing of **Cr-FF$_{OEt}$** in the crystalline lattice. **Figure 5d** shows a packing model based on the pseudo-orthorhombic unit cell with 2_1 symmetry along the *b*-axis. The unit cell contains two **Cr-FF$_{OEt}$** molecules with the diphenylalanine moiety in a flat conformation and the coronene moiety tilted by ca. 45° about the *a*-axis. These two molecules are related by the 2_1 symmetry. The structure forms through two strong molecular Interactions along the *c*-axis, the H-bonding of diphenylalanine moieties and the π-stacking of coronene moieties. As shown in **Figure 5d**, the amide groups form intermolecular H-bonds along the *c*-axis (red dashed lines in the *bc* projection). The tilt of coronene moiety allows them to form π-π interactions along the *c*-axis (violet bidirectional arrows). Compared to the *c*-axis, the molecules are relatively weakly associated along the other two axes through van der Waals interactions, mainly C-H···π interactions. The simulated diffraction pattern based on this model is in good agreement with the experimental ED pattern, supporting the soundness of the model (**Figure 5c**).

The FT-IR spectrum of **Cr-FF$_{OEt}$** in $CDCl_3$ exhibited peaks at 3424 cm^{-1} and 1668 cm^{-1}, corresponding to the symmetric N-H stretching vibration (amide A) and C=O stretching vibration (amide I). The nonclassical crystallization process induced shifts of the amide A band to 3282 cm^{-1} and the amide I band ($\upsilon_{C=O}$) to 1638 cm^{-1} (**Figure S17**).[19] These spectral changes corroborate the observed intermolecular H-bonds between the amide moieties in the 3D ED-based molecular model.

2.3. Assembly mechanism governed by intermolecular interactions

The ED analysis shows that the *c*-axis is along the fiber axis of the crystallites. The crystallization is, therefore, faster along the *c*-axis than in other crystallographic directions. This observation suggests that the two strong interactions, the H-bonds and the π-stacking interactions drive the initial stage of the crystallization of **Cr-FF$_{OEt}$**. Indeed, the poorly resolved ED pattern after 5 min of aging (Figure 3a) already exhibited the smeared reflections with a periodicity of 4.9 Å, corresponding to the spacing between H-bonded diphenylalanine residues.[20] However, the pronounced impact of the hydrophobic interaction of coronene moieties towards the later stages of the assembly process resulted in the formation of flat ribbons. Even though a similar formation of H-bonded structures occurred in the **Py-FF$_{OEt}$** system, the H-bond-driven helical organization[21] of the pyrene moieties was prominent in **Py-FF$_{OEt}$** compared to that of the **Cr-FF$_{OEt}$** (**Figure S18, 19**).

Circular dichroism (CD) studies provided further insight into the molecular packing and the possible induced chiral imprint of the dipeptide unit into the chromophore (Figure 6a).[22] The molecules were CD silent in the monomerically dissolved state. However, upon aggregation **Cr-FF$_{OEt}$**, and **Py-FF$_{OEt}$** showed CD patterns with varying intensity and pattern. The intensity of the CD signal is often found to be dependent on the rotational degree of chromophores, the reduced CD intensity of **Cr-FF$_{OEt}$** compared to that of **Py-FF$_{OEt}$** aggregates, shows the restricted impact of the peptide H-bonding network, thereby asymmetry transfer over the packing of coronene.

To further evaluate the required hydrophobic/hydrophilic balance of the molecule in predicting the surface topology, we thought to hydrolyze the terminal ester group of **Cr-FF$_{OEt}$**. Interestingly **Cr-FF** in water/ DMSO (8:2 v/v, $c_T = 5 \times 10^{-5}$ M) showed a well-defined exciton-coupled CD with an increased intensity compared to that of **Cr-FF$_{OEt}$** aggregates (**Figure 6a** and **Figure S20**). To corroborate the observed CD spectral changes the aggregate showed right-handed twisted nanoribbons with a width of 60 ± 20 nm and lengths of several micrometers (**Figure 6b,c**). This observation of the **Cr-FF** aggregation behavior highlights the delicate nature of the nonclassical crystallization of **Cr-FF$_{OEt}$**.

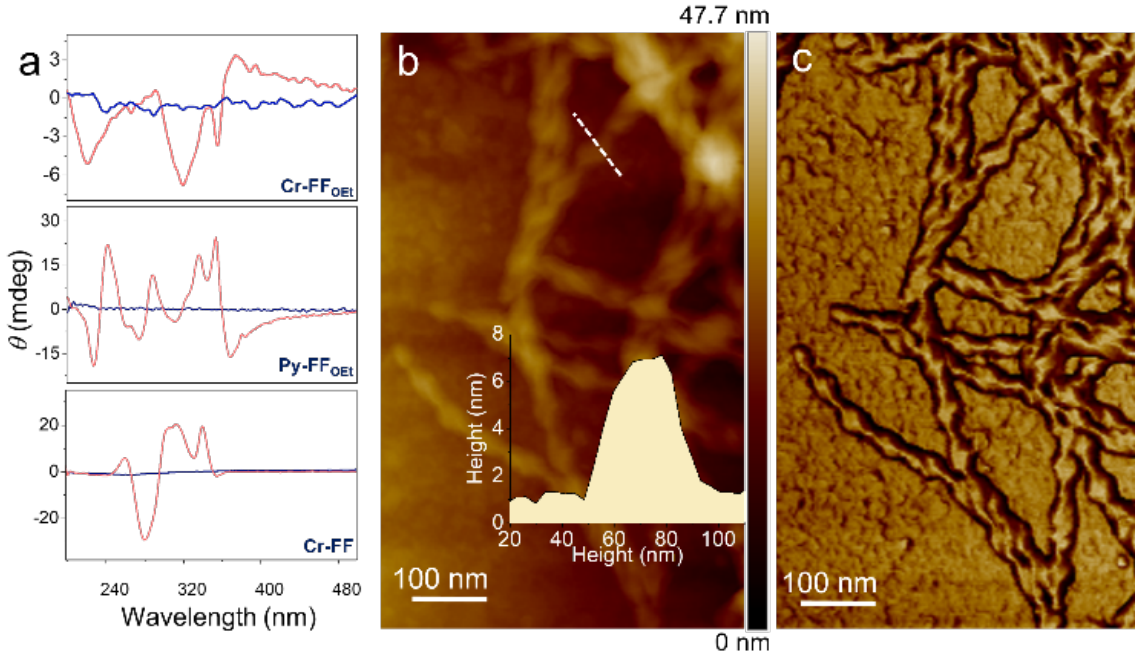

Figure 6. (a) CD spectrum of **Cr-FF$_{OEt}$** in THF, aggregates in water/THF (6:4 v/v, $c_T = 5 \times 10^{-5}$ M) at 25 °C (upper panel), **Py-FF$_{OEt}$** in THF, aggregates in water/THF (7:3 v/v, $c_T = 5 \times 10^{-5}$ M) at 25 °C (middle panel) and **Cr-FF** in DMSO, aggregates in water/DMSO (8:2 v/v, $c_T = 5 \times 10^{-5}$ M) at 25 °C (lower panel). The blue and red spectral lines indicate the monomerically dissolved and the aggregated states, respectively. (b) AFM height image of **Cr-FF** helical nanoribbons in water/DMSO (8:2 v/v, $c_T = 5 \times 10^{-5}$ M) at 25 °C. inset shows the height profile corresponding to the white dotted line. and (c) the corresponding phase image.

2.4. Mechanical and optoelectronic properties of mesocrystals

In accordance with the observed layered structural features, the microcrystal showed elastic, flexible behavior. Along with the one-dimensional (1D) array of strong π-stacking and the H-bonding interactions, a multitude of weak, dispersive interactions in the other two directions might be acting as the structural buffer for the deformation (**Figure S21**).[23]

The optoelectronic properties of the **Cr-FF$_{OEt}$** microcrystals were studied by flash-photolysis time-resolved microwave conductivity (FP-TRMC).[24] Upon excitation of the microcrystals of **Cr-FF$_{OEt}$** with a laser pulse of 355 nm produced transient conductivity, given by $\varphi\Sigma\mu$ (φ, photocarrier generation yield; $\Sigma\mu$ sum of the mobilities of photogenerated charge carriers) was observed. The maximum transient conductivity was estimated to be 1.40 $\times 10^{-4}$ cm^2 V^{-1} s^{-1} which is a 3.5 times enhancement in the conductivity compared to **Cr-FF$_{OEt}$** in its powdered form obtained by drying THF solution. Similarly, we have measured the transient conductivity for **Py-FF$_{OEt}$**. The fibrous assembly of **Py-FF$_{OEt}$** showed a 1.4 times lesser conductivity compared to that of the powdered form obtained by drying THF solution, due to the peptide-driven helical stacking of the pyrene moieties (**Figure 7**). The pronounced π-orbital interactions, as observed from the increased photoluminescence lifetime of the **Cr-FF$_{OEt}$** microcrystals, further support the increased conductivity. The results emphasize the significance of the fundamental particulate character of microcrystals, as well as the importance of shaping the energy landscape to obtain optimal material properties.

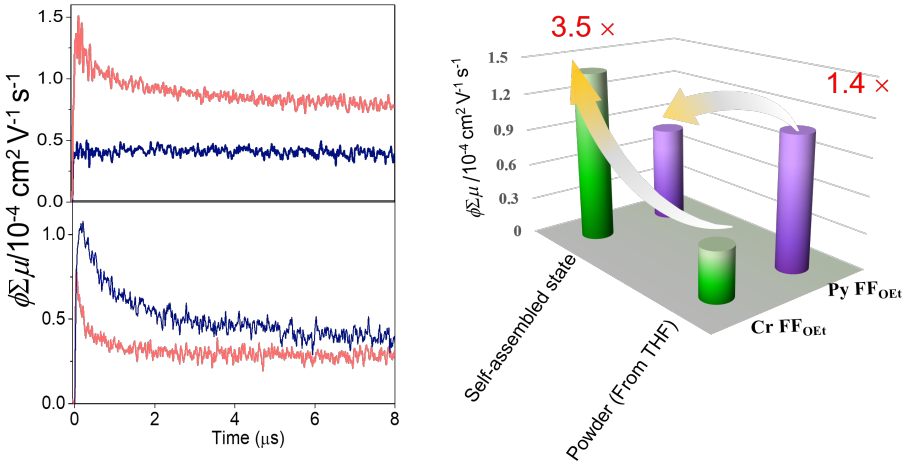

Figure 7. (a) Transient photoconductivity (FP-TRMC) profiles of **Cr-FF$_{OEt}$** (top panel), **Py-FF$_{OEt}$** (bottom panel), self-assembled state (red), powder form dried from THF (blue). (b) Plot showing the variation of $\phi\Sigma\mu$ maxima.

3. Conclusion

In summary, we have demonstrated the nonclassical crystal growth of supramolecular polymers of a coronene-dipeptide conjugate (**Cr-FF$_{OEt}$**). The detailed spectroscopic, microscopic, and crystallographic characterization revealed the structural and morphological evolutions of **Cr-FF$_{OEt}$** from hairy imperfect 1D nanofibers to micron-sized crystalline ribbons. The lateral interactions among these 1D structures resulted in the spontaneous growth across multiple length scales leading to mesoscale crystals. 3D ED analysis showed that peptide H-bonding and the π-stacking of coronene units drove the formation of the fibrillar assemblies. The observed intermediates of the nonclassical crystallization pathway were found to be quite flexible in optimizing the intermolecular interactions to accommodate the impending structural changes. The modifications in the molecular structure of **Cr-FF$_{OEt}$** resulted in distinct supramolecular assembly behaviors, as **Py-FF$_{OEt}$** and **Cr-FF** formed helical and twisted fibers, respectively. The difference in the assembly manners of the three molecules highlights the delicate balance of intermolecular interactions governing the nonclassical crystal growth process of **Cr-FF$_{OEt}$**. A thorough understanding of the system is pivotal in balancing the H-bonding and hydrophobic interactions for creating supramolecular structures with appropriate surface topology in aqueous media. Further precise internal ordering of supramolecular polymers makes them potential building blocks (supramolecular elements)[7,25] for the next step in the hierarchy of organizations, a formidable challenge in synthetic supramolecular materials.

Supporting Information

Supporting Information is available from the Wiley Online Library or from the author.

Acknowledgments

D.E. acknowledges CSIR, Government of India, for a research fellowship. J.H.L., Y.N., and Y.O. acknowledge Agence Nationale de la Recherche (ANR grant number: ANR-21-CE29-0016-1) for the financial support and the NanoBio-ICMG platform (FR 2607) for granting access to the electron microscopy facility. V.K.P. is grateful to the Council of Scientific and Industrial Research (CSIR), Government of India and Department of Science and Technology (DST), Nano Mission, Government of India (DST/NM/TUE/EE-02/2019), for the financial support. D.E. and V.K.P. thank Ms. Soumini Mathew, Ms. Viji S., and Mr. Kiran Mohan (CSIR-NIIST) for their experimental support.

[1] a) C. B. Anfinsen, *Science* **1973**, *181*, 223–230; b) W. Saenger, *Principles of Nucleic Acid Structure*, Springer, New York, **1984**; c) C. M. Dobson, *Nature* **2003**, *426*, 884–890.

[2] a) O. J. G. M. Goor, S. I. S. Hendrikse, P. Y. W. Dankers, E. W. Meijer, *Chem. Soc. Rev.* **2017**, *46*, 6621–6637; b) M. P. Hendricks, K. Sato, L. C. Palmer, S. I. Stupp, *Acc. Chem. Res.* **2017**, *50*, 2440–2448; c) P. K. Hashim, J. Bergueiro, E. W. Meijer, T. Aida, *Prog. Polym. Sci.* **2020**, *105*, 101250.

[3] a) E. Krieg, M. M. C. Bastings, P. Besenius, B. Rybtchinski, *Chem. Rev.* **2016**, *116*, 2414–2477; b) S. Dhiman, S. J. George, *Bull. Chem. Soc. Jpn*. **2018**, *91*, 687–699; c) F. Sheehan, D. Sementa, A. Jain, M. Kumar, M. Tayarani-Najjaran, D. Kroiss, R. V Ulijn, *Chem. Rev.* **2021**, *121*, 13869–13914; d) S. Datta, S. Takahashi, S. Yagai, *Acc. Mater. Res.* **2022**, *3*, 259–271.

[4] a) A. Sorrenti, J. Leira-Iglesias, A. J. Markvoort, T. F. A. de Greef, T. M. Hermans, *Chem. Soc. Rev.* **2017**, *46*, 5476–5490; b) J. Matern, Y. Dorca, L. Sánchez, G. Fernández, *Angew. Chem. Int. Ed.* **2019**, *58.* c) M. Wehner, F. Würthner, *Nat. Rev. Chem.* **2020**, *4*, 38–53.

[5] a) P. A. Korevaar, S. J. George, A. J. Markvoort, M. M. J. Smulders, P. A. J. Hilbers, A. P. H. J. Schenning, T. F. A. De Greef, E. W. Meijer, *Nature* **2012**, *481*, 492–496; b) F. Tantakitti, J. Boekhoven, X. Wang, R. V. Kazantsev, T. Yu, J. Li, E. Zhuang, R. Zandi, J. H. Ortony, C. J. Newcomb, L. C. Palmer, G. S. Shekhawat, M. O. de la Cruz, G. C. Schatz, S. I. Stupp, *Nat. Mater.* **2016**, *15*, 469–476; c) M. Wehner, M. I. S. Röhr, M. Bühler, V. Stepanenko, W. Wagner, F. Würthner, *J. Am. Chem. Soc.* **2019**, *141*, 6092–6107; d) B. Kemper, L. Zengerling, D. Spitzer, R. Otter, T. Bauer, P. Besenius, *J. Am. Chem. Soc.* **2018**, *140*, 534–537.

[6] a) A. Lohr, M. Lysetska, F. Würthner, *Angew. Chem. Int. Ed.* **2005**, *44*, 5071–5074 b) S. H. Jung, M. Takeuchi, K. Sugiyasu, in *Kinetic Control in Synthesis and Self-Assembly,* (Eds.: M. Numata, S. Yagai, T. Hamura), Academic Press, **2019**, pp. 205–229; c) K. Sugiyasu, in *Out ‐ of ‐ Equilibrium (Supra)molecular Systems and Materials*, (Eds.: N. Giuseppone, A. Walther), WILEY-VCH GmbH, Weinheim, **2021**, pp. 131–164.

[7] a) J. M. Lehn, *Angew. Chem. Int. Ed.* **2013**, *52*, 2836–2850. b) G. Vantomme, E. W. Meijer, *Science* **2019**, *363*, 1396–1397; c) K. Ariga, T. Mori, T. Kitao, T. Uemura, *Adv. Mater.* **2020**, *32*, 1905657.

[8] a) H. Cölfen, S. Mann, *Angew. Chem. Int. Ed.* **2003**, *42*, 2350–2365. b) P. G. Vekilov, *J. Cryst. Growth* **2005**, *275*, 65–76; c) H.-B. Yao, H.-Y. Fang, X.-H. Wang, S.-H. Yu, *Chem. Soc. Rev.* **2011**, *40*, 3764–3785; d) L. Bahrig, S. G. Hickey, A. Eychmüller, *CrystEngComm* **2014**, *16*, 9408–9424; e) C. Yuan, W. Ji, R. Xing, J. Li, E. Gazit, X. Yan, *Nat. Rev. Chem.* **2019**, *3*, 567–588; f) M. Jehannin, A. Rao, H. Cölfen, *J. Am. Chem. Soc.* **2019**, *141*, 10120–10136.

[9] a) J. Hwang, T. Heil, M. Antonietti, B. V. K. J. Schmidt, *J. Am. Chem. Soc.* **2018**, *140*, 2947–2956; b) I. Nemtsov, Y. Mastai, M. Ejgenberg, *Cryst. Growth Des*. **2018**, *18*, 4054–4059; c) C. Bortolini, L. H. Klausen, S. V. Hoffmann, N. C. Jones, D. Saadeh, Z. Wang, T. P. J. Knowles, M. Dong, *ACS Nano* **2018**,

12, 5408–5416; d) L. Adler-Abramovich, Z. A. Arnon, X. Sui, I. Azuri, H. Cohen, O. Hod, L. Kronik, L. J. W. Shimon, H. D. Wagner, E. Gazit, *Adv. Mater.* **2018**, *30*, 1704551; e) Z. Chen, K. Higashi, K. Ueda, K. Moribe, *Nano Lett.* **2022**, *22*, 6841–6846.

[10] a) C. E. Killian, R. A. Metzler, Y. U. T. Gong, I. C. Olson, J. Aizenberg, Y. Politi, F. H. Wilt, A. Scholl, A. Young, A. Doran, M. Kunz, N. Tamura, S. N. Coppersmith, P. U. P. A. Gilbert, *J. Am. Chem. Soc.* **2009**, *131*, 18404–18409; b) Y. U. T. Gong, C. E. Killian, I. C. Olson, N. P. Appathurai, A. L. Amasino, M. C. Martin, L. J. Holt, F. H. Wilt, P. U. P. A. Gilbert, *Proc. Natl. Acad. Sci. U. S. A.* **2012**, *109*, 6088–6093.

[11] a) S. L. Burkett, M. E. Davis, *Chem. Mater.* **1995**, *7*, 920–928; b) J. P. Grotzinger, N. P. James, *Carbonate Sedimentation and Diagenesis in the Evolving Precambrian World*, SEPM Society for Sedimentary Geology, Tulsa, Vol. 67, **2000**.

[12] a) W. J. E. M. Habraken, J. Tao, L. J. Brylka, H. Friedrich, L. Bertinetti, A. S. Schenk, A. Verch, V. Dmitrovic, P. H. H. Bomans, P. M. Frederik, J. Laven, P. van der Schoot, B. Aichmayer, G. de With, J. J. DeYoreo, N. A. J. M. Sommerdijk, *Nat. Commun.* **2013**, *4*, 1507; b) Y. Tsarfati, S. Rosenne, H. Weissman, L. J. W. Shimon, D. Gur, B. A. Palmer, B. Rybtchinski, *ACS Cent. Sci.* **2018**, *4*, 1031–1036; c) I. Biran, S. Rosenne, H. Weissman, Y. Tsarfati, L. Houben, B. Rybtchinski, *Cryst. Growth Des.* **2022**, *22*, 6647–6655.

[13] a) S. Chung, S.-H. Shin, C. R. Bertozzi, J. J. De Yoreo, *Proc. Natl. Acad. Sci. U. S. A.* **2010**, *107*, 16536–16541; b) F. Tao, Q. Han, K. Liu, P. Yang, *Angew. Chem. Int. Ed.* **2017**, *56*, 13440–13444. c) X. Ma, S. Zhang, F. Jiao, C. J. Newcomb, Y. Zhang, A. Prakash, Z. Liao, M. D. Baer, C. J. Mundy, J. Pfaendtner, A. Noy, C.-L. Chen, J. J. De Yoreo, *Nat. Mater.* **2017**, *16*, 767–774; d) F. Tao, Q. Han, P. Yang, *Langmuir* **2019**, *35*, 183–193.

[14] a) P. C. Ke, R. Zhou, L. C. Serpell, R. Riek, T. P. J. Knowles, H. A. Lashuel, E. Gazit, I. W. Hamley, T. P. Davis, M. Fändrich, D. E. Otzen, M. R. Chapman, C. M. Dobson, D. S. Eisenberg, R. Mezzenga, *Chem. Soc. Rev.* **2020**, *49*, 5473–5509; b) Reynolds, N. P.; Adamcik, J.; Berryman, J. T.; Handschin, S.; Zanjani, A. A. H.; Li, W.; Liu, K.; Zhang, A.; Mezzenga, R. Competition between Crystal and Fibril Formation in Molecular Mutations of Amyloidogenic Peptides. *Nat. Commun.* **2017**, *8* 1338.

[15] a) T. Gruene, J. J. Holstein, G. H. Clever, B. Keppler, *Nat. Rev. Chem.* **2021**, *5*, 660–668; b) T. Gruene, E. Mugnaioli, *Chem. Rev.* **2021**, *121*, 11823–11834; c) L. Samperisi, X. Zou, Z. Huang, *CrystEngComm* **2022**, *24*, 2719–2728; d) Y. Ogawa, J.-L. Putaux, *Front. Chem.* **2022**, *10*, 835663.

[16] a) S. Gim, G. Fittolani, Y. Nishiyama, P. H. Seeberger, Y. Ogawa, M. Delbianco, *Angew. Chem. Int. Ed.* **2020**, *59*, 22577–22583. b) M. Ueda, T. Aoki, T. Akiyama, T. Nakamuro, K. Yamashita, H. Yanagisawa, O. Nureki, M. Kikkawa, E. Nakamura, T. Aida, Y. Itoh, *J. Am. Chem. Soc.* **2021**, *143*, 5121–5126; c) K. Kato, K. Takaba, S. Maki-Yonekura, N. Mitoma, Y. Nakanishi, T. Nishihara, T. Hatakeyama,

T. Kawada, Y. Hijikata, J. Pirillo, L. T. Scott, K. Yonekura, Y. Segawa, K. Itami, *J. Am. Chem. Soc.* **2021**, *143*, 5465–5469.

[17] a) K. Ohno, H. Inokuchi, T. Kajiwara, *Bull. Chem. Soc. Jpn.* **1972**, *45*, 996–1004; b) N. Nijegorodov, R. Mabbs, W. S. Downey, *Spectrochim. Acta, Part A* **2001**, *57*, 2673–2685; c) K. Takazawa, J.-i. Inoue, K. Mitsuishi, *Nanoscale* **2014**, *6*, 4174–4181.

[18] a) K. Balakrishnan, A. Datar, R. Oitker, H. Chen, J. Zuo, L. Zang, *J. Am. Chem. Soc.* **2005**, *127*, 10496–10497; b) X. Yan, Y. Su, J. Li, J. Früh, H. Möhwald, *Angew. Chem. Int. Ed.* **2011**, *50*, 11186–11191.

[19] a) W. K. Surewicz, H. H. Mantsch, *Biochim. Biophys. Acta, Protein Struct. Mol. Enzymol.* **1988**, *952*, 115–130; b) M. J. Winningham, D. Y. Sogah, *Macromolecules* **1997**, *30*, 862–876; c) W. Ji, C. Yuan, P. Chakraborty, S. Gilead, X. Yan, E. Gazit, *Commun. Chem.* **2019**, *2*, 65; d) F. N. Barrera, *Arch. Biochem. Biophys.* **2022**, *726*, 109114.

[20] R. Nelson, M. R. Sawaya, M. Balbirnie, A. Ø. Madsen, C. Riekel, R. Grothe, D. Eisenberg, *Nature* **2005**, *435*, 773–778.

[21] a) A. Sarbu, L. Biniek, J. M. Guenet, P. J. Mésini, M. Brinkmann, *J. Mater. Chem. C* **2015**, *3*, 1235–1242; b) G. Das, R. Thirumalai, B. Vedhanarayanan, V. K. Praveen, A. Ajayaghosh, *Adv. Opt. Mater.* **2020**, *8*, 2000173.

[22] a) N. Harada, K. Nakanishi, S. Tatsuoka, *J. Am. Chem. Soc.* **1969**, *91*, 5896–5898; b) N. Harada, S.-M. L. Chen, K. Nakanishi, *J. Am. Chem. Soc.* **1975**, *97*, 5345–53521.

[23] a) P. Naumov, S. Chizhik, M. K. Panda, N. K. Nath, E. Boldyreva, *Chem. Rev.* **2015**, *115*, 12440–12490; b) W. M. Awad, D. W. Davies, D. Kitagawa, J. Mahmoud Halabi, M. B. Al-Handawi, I. Tahir, F. Tong, G. Campillo-Alvarado, A. G. Shtukenberg, T. Alkhidir, Y. Hagiwara, M. Almehairbi, L. Lan, S. Hasebe, D. P. Karothu, S. Mohamed, H. Koshima, S. Kobatake, Y. Diao, R. Chandrasekar, H. Zhang, C. C. Sun, C. Bardeen, R. O. Al-Kaysi, B. Kahr, P. Naumov, *Chem. Soc. Rev.* **2023**, 3098–3169.

[24] a) A. Saeki, Y. Koizumi, T. Aida, S. Seki, *Acc. Chem. Res.* **2012**, *45*, 1193–1202; b) S. Seki, A. Saeki, T. Sakurai, D. Sakamaki, *Phys. Chem. Chem. Phys.* **2014**, *16*, 11093–11113.

[25] H. Schmidt, F. Würthner, *Angew Chem. Int. Ed.* **2020**, *59*, 8766–8775

[26] S. Matsumura, A. R. Hlil, C. Lepiller, J. Gaudet, D. Guay, Z. Shi, S. Holdcroft, A. S. Hay, *J. Polym. Sci., Part A: Polym. Chem.* **2008**, *46*, 7207–7224.

[27] L. Davenport, B. Shen, T. W. Joseph, M. P. Straher, *Chem. Phys. Lipids* **2001**, *109*, 145–156.

[28] B. Adhikari, J. Nanda, A. Banerjee, *Chem. Eur. J.* **2011**, *17*, 11488–11496.

Entry for the Table of Contents

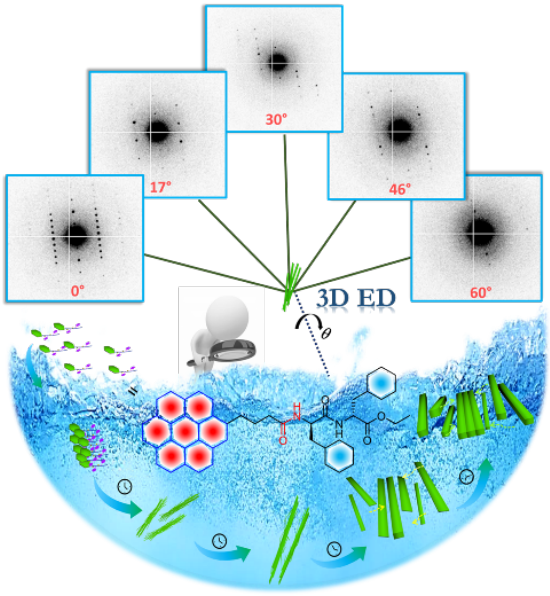

The concept of nonclassical crystallization is applied to the fibril-to-crystal conversation of a supramolecular polymer. Gradual optimization of the intermolecular interactions and the favorable surface topology of the intermediates were found to be critical in the facile creation of a complex form of hierarchy.

Institute and/or researcher Twitter usernames: @csir_niist

Revised: ((will be filled in by the editorial staff))

Published online: ((will be filled in by the editorial staff))